

Nonlinear 3D finite element modelling of conventional and composite steel spaceframes structures

Haitham H. Muteb¹, Harith Al-Salman²

¹ Lecturer, Department of Civil Engineering, University of Babylon, Collage of Engineering

² Student, Department of Civil Engineering, University of Babylon, Collage of Engineering

ABSTRACT

Spaceframes steel structures are a common worldwide technique for roofing wide areas. In this study, after validating one of the models experimentally, nonlinear 3d finite element modelling was performed to analyze failure mechanism of space frames models with the help of Abaqus program. Additionally, this study attempts to convert such common roofing structure to a composite structure using ultra high strength concrete slab to withstand various floor loads. Various space frames shaft angles were tested, namely, 30, 45, and 60. Tests results were evaluated and compared in term of ultimate load, load at maximum displacement, toughness, and stiffness. Tests results have shown that spaceframes models with angle 60 have the highest load capacity compared to other angles, and highest toughness compared to various techniques. Also, compositing 40 mm of ultra-high-performance concrete slab method has approved its efficiency to withstand loads and showed comparable results with the conventional spaceframes. The composite systems with sufficient concrete slab thickness and strength have reflected an efficient technique for flooring wide span structures.

Keywords: Spaceframes, concrete Composite Spaceframes, Ultra high-performance concrete, Finite element Analysis, Abaqus.

Corresponding Author:

Harith Al-Salman,
Department of Civil Engineering,
College of Engineering, University of Babylon,
Babylon, Iraq.
E-mail: harithsama@yahoo.com

1. Introduction

Space truss roof systems have widely been used to cover large areas because of their less weight. A special type of space truss roof, called Mero space truss roof, has often been employed since the use of prefabricated straight tubular elements with bolts and sleeves (truss bars) and a sphere (Mero node) designed in so as to allow connection among the truss bars, make the handling and assembly work easier [1].

Despite of the advantages of the space truss roof systems mentioned above, these types of systems are very prone to progressive collapse initiated by buckling of the truss bars. In particular, a space truss roof in which the buckled truss bars gather in a certain region across the roof may entirely collapse suddenly without any indication and warning [2]. A numerical investigation on the progressive collapse behavior of double-layer space truss roofs has proved the sensitivity of these structures against the progressive collapse when subjected to increasing applied load. However, even though some truss bars buckle in flexural mode, the entire roof may not collapse because the system is capable of allowing redistribution of axial forces to a small extent [3].

For instance, if a space truss roof is subjected to soil-induced settlements resulting in disproportionately relative displacements among the roof supports in time, axial force redistribution in truss bars is likely, but still limited to negligible level.

Many researches have been conducted on the investigation of collapse behaviors of the space truss roof systems. One has reported the investigation of a space truss roof designed to cover a reinforced building that has totally collapsed due to snow load initially underestimated and some mistakes made in the design [4]. Additionally, the partial collapse of a space truss roof of an industrial plant has been investigated in [4] and it has been reported that the collapse was because of ice ponds after exceptional snow load. Another research [5] has addressed a long-span steel roof structure collapsed during construction as a result of an out-of-plane buckling phenomenon caused by a gust of wind. The partial collapse of a space truss roof structure that occurred during strong winds and heavy rains was investigated based on the site observation and experimental study on the bolts [6]. An experimental study was performed to investigate the ductility behavior of a space truss roof system that consists of cold-formed hollow square sections attached to a joint through the special welded joint plates and bolted connections [7]. A methodology allowing to perform nonlinear post buckling analysis of space truss systems was developed and applied to double-layer space truss to obtain the vertical load displacement response [8]. A numerical research based on a nonlinear stepwise linearization analysis method was carried out to investigate the nonlinear behavior of space truss members [9].

This study aims to evaluate and identify numerically failure capacity of various spaceframes systems, and check their ability to withstand floor loads through connecting a concrete slab layer made with plain ultra-high-performance concrete (UHPC) to the conventional space frame.

2. Description of the FEM models

Three different type of conventional SF models were adopted to simulate in this study after checking validity with specimen SF-A45. Each model has different angle between hallow circular members, they are; angle 30, 45, and 60. Each specimen was designated with a code as listened in table (1). As a result of variable angle of connected members, the spaceframes heights were also varied, started from 302 mm for SF-A30, to 514 mm for SF-A60. All SFs cord members dimensions are the same in top view direction. While the diagonal members were varied based on SF height. In general, the joint steel ball was with 90 mm diameter, the thickness of used hallow circular section was about 2 mm, and outer diameter of 42 mm. The total length of SFs c/c of balls was about 1200 mm, and of 600 mm c/c of ball in width.

The same dimensions were adopted for Composite spaceframes models, which also have designated with codes as mentioned in table (1). The CSFs have the same dimensions mentioned previously in SFs models, except two main difference; The first, is the concrete deck slab of dimensions 700 mm width, 1300 mm length, and 40 mm thickness. The second, is the steel supporting plate placed under deck slab and above ball joints. The corner square plates were with dimensions of 100 mm and 10 mm, for length and thickness, respectively. While the mid support plates were with dimensions of 125x150x10 mm, for length, width, and thickness, respectively. It worth to be mentioned that all parts dimensions were selected according to what available locally. Figures 1.a and 1.b illustrates typical models' configurations in 2D view, Figure 2a and 2b illustrated typical FEA models configurations in 3D view.

Table 1. Specimens designations

SPECIMENS DESIGNATION	TYPE OF SPACE FRAME	ANGLE BETWEEN SHAFT MEMBERS
SF-A30	Non composite	30
SF-A45	Non composite	45
SF-A60	Non composite	60
CSF-A30	composite	30
CSF-A45	composite	45
CSF-A60	composite	60



Figure 1. Testing configurations for SF-A45 specimens

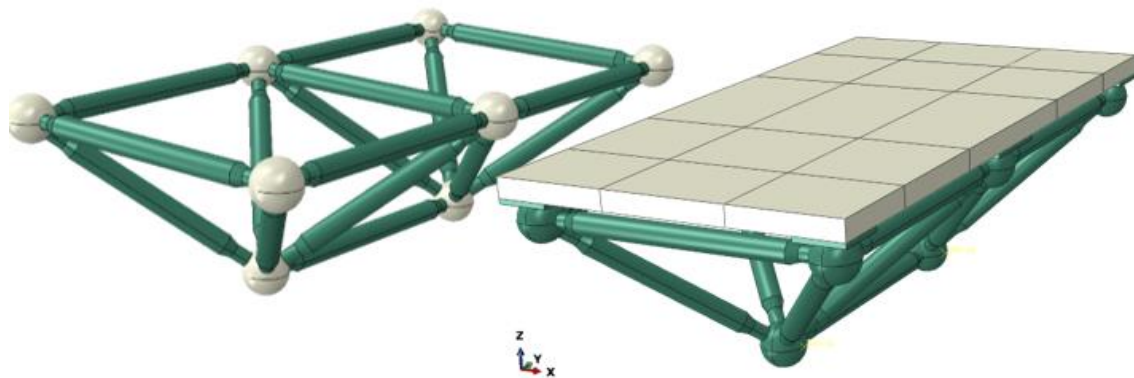


Figure 2. FEM typical model's configurations for SF models (the the left), and CSF models (at the right) in 3D view

3. Finite element modelling with Abaqus

Abaqus is a finite element simulation software that have wide population in various civil engineering applications, espically for structural engineering. It is necessary to define materil models to get the desirable behaviour of the overall structure, as shall be described in next subsections.

3.1. Materials characteristics and modelling

Lubliner et al [10] had predicted One of the important models that has covered by Abaqus, which is called the concrete damage plasticity model (CDP). The model then modified by Lee and Fenves [11]. The CDP model is a continuum based on the theory of plasticity which assumes tow failure criteria are, the compressive crushing and tension stiffening.

The Adopted Concrete Material characteristics were selected according to reference [12], where Ultra high-performance concrete with steel fiber was used. The maximum concrete compressive strength was illustrated in the stress- strain curve relationship in Figure (3), which was about 124 MPa. Also, rapture strength was about and 30 MPa.

All mentioned chrematistics were refined and edited as CDP parameters required. A bilinear relation of tensile stress- displacement were assigned, as illustrated in Figure (3). While compressive curve characteristics beyond the elastic limit were defined as can be seen in Figure (4), since Abaqus takes the elastic limit from modulus of elasticity value.

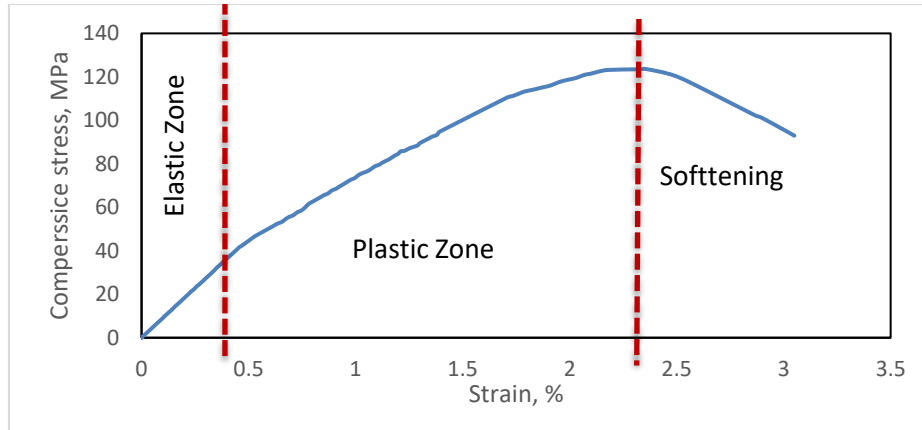


Figure 3. Raw compressive Stress-Strain relation of UHPC [12]

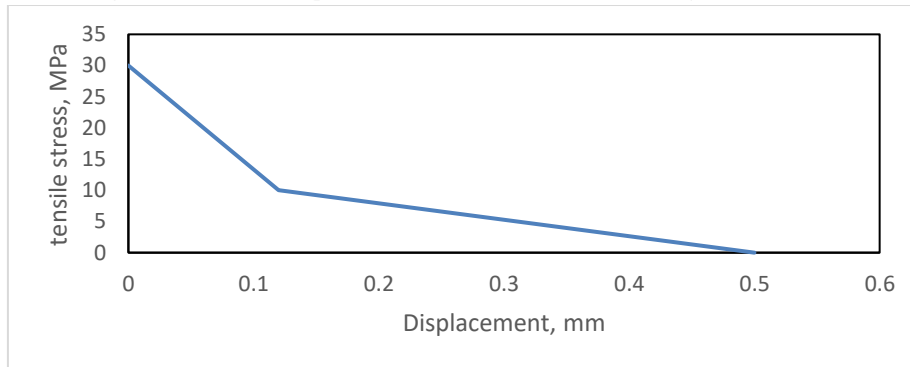


Figure 4. tensile Stress-displacement relation of UHPC [12]

The concrete damage plasticity model was selected for concrete material modelling. Such model approved its efficiency to simulate the brittle concrete deck slab behavior. The adopted parameters of CDP model are listed in Table (2). The passion’s ratio of UHPC is lower than value of normal concrete, which was selected as recommended by reference [13]. Further, several researchers reported that dilation angle of concrete increases proportionally with its performance. The selected dilation angle was about 40 as recommended by [14]. Other parameters were selected such as ratio of biaxial to uniaxial stress (f_{b0}/f_c), and plasticity number (K) were obtained using referred formulas in Table (2), and some values were selected by default from Abaqus user manual. For Passion’s ratio parameter, according to FIB model code, it ranges between 0.1-0.2 for ranges of stresses between $0.5f'_c$ and f'_c . the value of 0.15 The Eurocode 2 [15] specifies the modulus of elasticity for concrete to be secant in a range of 0–0.4 f_c . Normally, the value ranges from 40 to 70 GPa[16]. Attention should be paid while inserting CDP parameters since such models requires each behavior of the concrete material to be input separately.

Table 2. Concrete Damage Plasticity parameters

Parameter	Selected value
Material model	CDP model
E, MPa	$E_c = 4700\sqrt{f'_c}$ [17]
Possions ratio	0.15
Dilation angle	40
Ecc	0.1*
f_{b0}/f_c	$f_{b0}/f'_c = 1.5(f'_c)^{-0.075}$ [18]
K	$Kc = 5.5/[5 + 2(f'_c)^{0.075}]$ [19]
Viscosity parameter	0.001 [20]

Note: * refers to a default value selected from Abaqus user’s manual.

For steel stress-strain curve, the behavior was predicted using Ramberg-Osgood Coefficients [21, 22], using steel properties as illustrated in table (3) utilizing from equations 1,2,3,4 and 5.

Table 3. Steel properties used in FEA modelling

property	Value, unit	
E	200,000	N/mm2
Ftu	487	N/mm2
Fty	389	N/mm2
e max	20	%

$$\epsilon_{us} = 100 \cdot \left(\epsilon_r - \frac{F_{tu}}{E} \right) \tag{1}$$

$$n = \frac{\text{Ln}(\epsilon_{us}/0.2)}{\text{Ln}(F_{tu}/F_{ty})} \tag{2}$$

ϵ_{us} = uniform strain = plastic strain at end of uniform elongation (at max. tension load Ftu)

n=20.63. Steel material stress-strain curve is calculated based on MMPDS-01[23], equation 9.8.4.1.2(b):

$$\epsilon = \frac{\sigma}{E} + 0.002 \cdot \left(\frac{\sigma}{F_{ty}} \right)^n \tag{3}$$

In finite element simulation, and to get more accurate results, engineering stress-strain curve should be corrected to the true stress- strain curve, to takes into account the reduction of area in tension using the basic Eq. (4) and (5).

$$\epsilon_{true} = \text{Ln}(1 + \epsilon) \tag{4}$$

$$\sigma_{true} = \sigma(1 + \epsilon) \tag{5}$$

Figure (5) illustrates the final stress-strain curve after applying the mentioned formula using adopted steel properties in table (3). both elastic and plastic behaviors of steel material model of true stress-strain relation were assigned to predict steel real behavior.

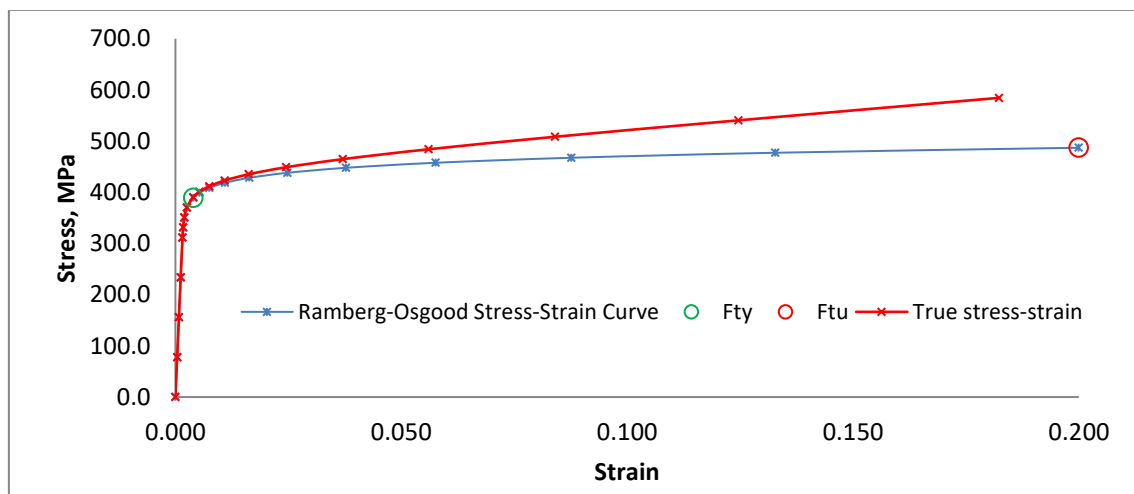


Figure 5. Predicted Stress-Strain Steel behavior

3.2. Meshing and type of elements

Meshing is a common matter for any model required to be simulated using finite element technique. Abaqus provide several elements types and shapes which each of them is suitable for a specified simulation purpose. for hollow circular members, a 10 mm linear quadrilateral elements of type S4R were assigned since it considers as a shell element. While for steel ball joints, a deformable 3D Quadratic tetrahedron type C3D10 were assigned. in case of CSFs, the same assignments were used, in addition to 3d deformable steel elements for the supporting plate of a Linear hexahedron mesh type, C3D8R. additionally, concrete deck slab were assigned with a 3D deformable element, an 8-node linear brick, reduced integration, hourglass control (C3D8R) of 30X30X2 mm brick element dimensions to reduce shear locking effect [24]. Figure (6) illustrates type of element for each part of the simulated models.

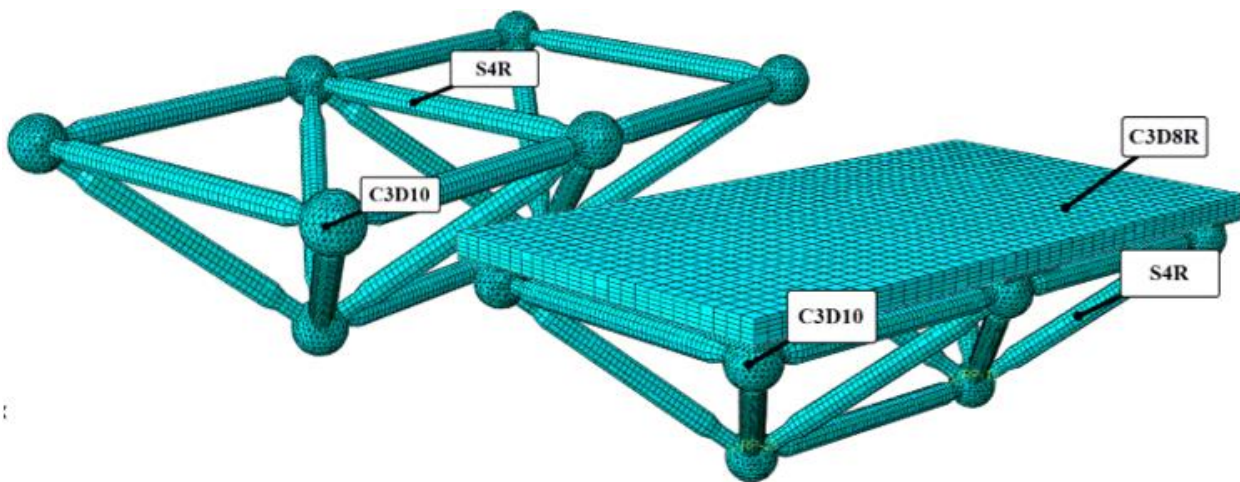


Figure 6. element types of meshing various models' parts

3.3. Boundary and loading conditions

Both bottom joints of SFs and CSFs models were fixed constrained using rigid body technique in Abaqus. The top square loading plates of length of 250 mm were normally contacted with the slab element, in addition to tangential contact behavior with frictional penalty factor of 0.3 [25]. loading plates were defined as rigid body using rigid body constrain technique. The latter technique is necessary to reduce computational time required to solve the problem [26]. A quasi-static loading type were used since static loading property cannot capture local or general buckling of long members of the SFs [27]. For conventional SFs, A vertical downward displacement of 50 mm was applied to the top head of the joints ball. While for CSFs models, displacement control type was applied to the top rigid plates with sufficient values to obtain both pre and post failure behavior. The contact type between supporting plates and concrete were treated as a fully bonded surfaces, using tie constrain type. Also, the same constrain was considered between the supporting plates and steel ball joints. Figure (7) illustrates loading and boundary conditions for both SFs and CSFs models.

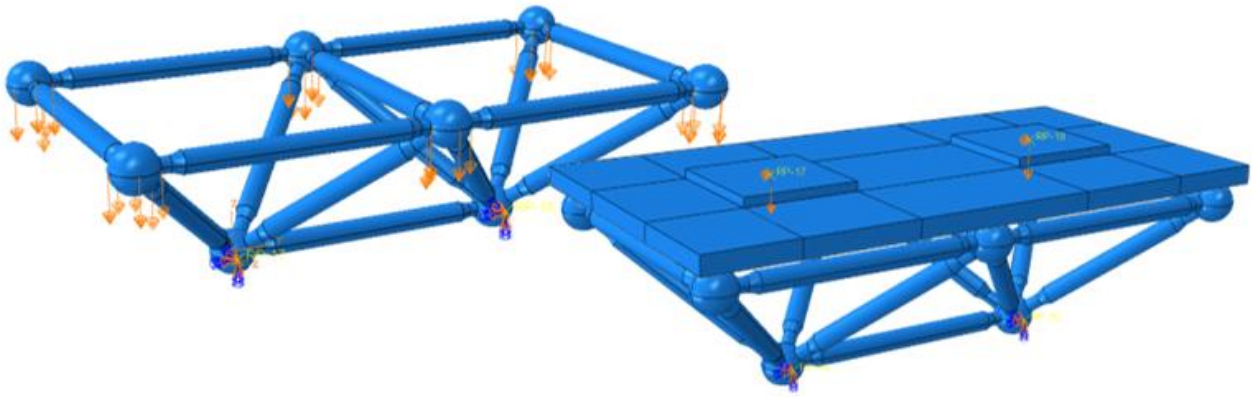


Figure 7. Boundary and loading conditions for both SFs and CSFs modes

4. Results of conventional spaceframes (SFs)

FEM simulation validity results of SF-A45 have shown a very close behavior to the experimental specimen, as illustrated in Figure (8). the maximum load was approximately the same, while the displacement at maximum load were slightly varied between them. As a result, the simulation process with all its mentioned details can be adopted to simulate other specimens.

The FEM simulation of the modelled specimens have shown different results for maximum load carrying capacity, where SP-A60 achieved maximum capacity among other models. While the SP-A30 has reflected the least load carry capacity, as clarified in Figure (9), in term of vertical applied load and mid displacement.

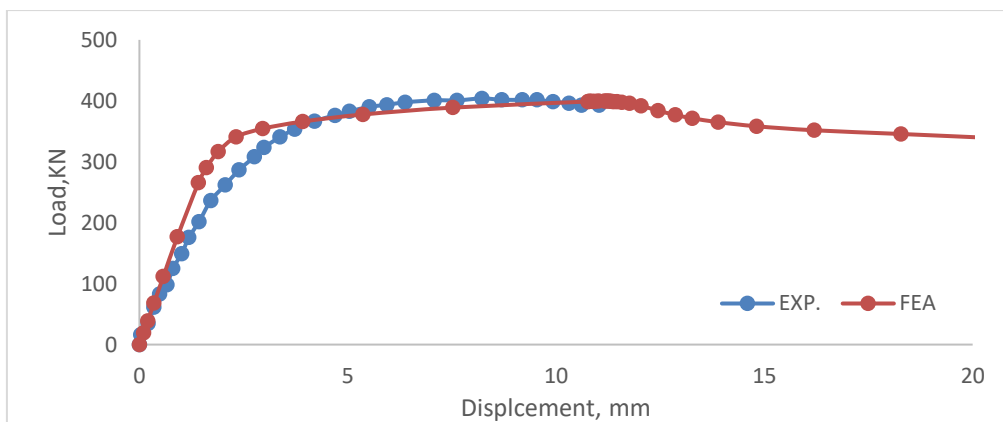


Figure 8. FEA Validation of B-SF-45 specimens

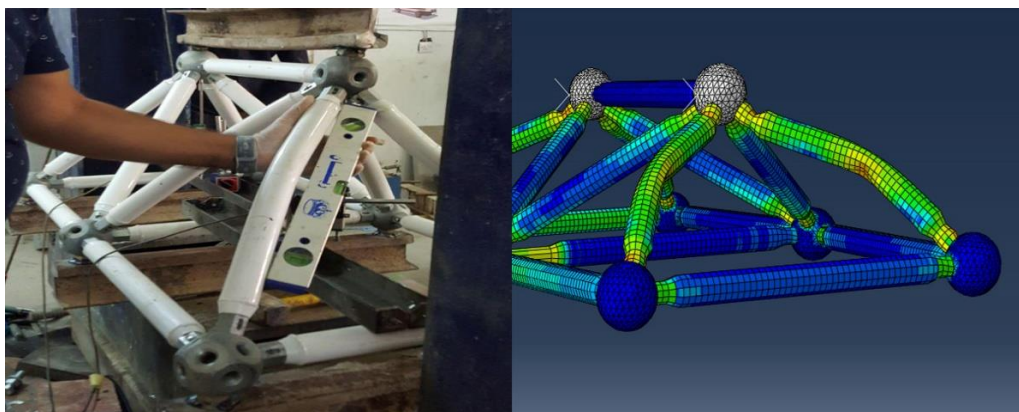


Figure 9: Failure Validation of B-SF-45 specimens

The maximum load obtained for SP-A60 was about 592.7 kN which corresponds to a vertical displacement of 13.05 mm, while the SP-A45 model has reflected a maximum load of about 391.82 kN corresponding to 12.04 mm vertical displacement. The SP-A30 model reflected the least capacity of about 238.8 kN at 11.33 mm vertical displacement. Further, a nonlinear proportional power relationship between SFs members angle and maximum load capacity, as observed from Figure (9). Increasing angle value about 15 degrees resulted in an average increase of 157.5% maximum capacity load.

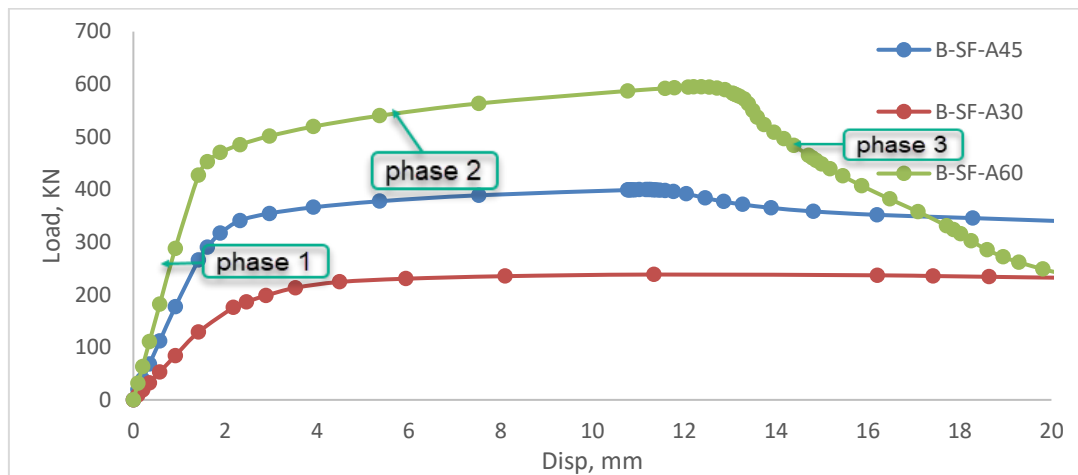


Figure 10. Load-Displacement curves relationship for various SFs models

Increasing members angle from 45 to 60 resulted in an increase in SF load capacity of about 150%, while about 165% increase when angle varies from 30 to 45. It can also be observed that the maximum carrying load for each model has approximately very close downward displacement compared to each other, which they are; 13.05 mm, 12.04 mm, and 11.33 mm for SP-A30, SP-A45, and SP-60, respectively.

On the other side, SP-A30 had the highest ductility compared to other models, while SP-A60 reflected the lowest ductility property among the models. The degradation behavior of SP-A60 models' curve was very sharp, on the contrary to what has been noticed in SP-A30 curve behavior, which was not easy to establish maximum load value due to curve smoothness after yielding. Further, SP-A45 models curve behavior had better performance than SP-A60 model. In terms of ductility, the maximum degradation value in load capacity was about 84.8%, 54%, and 26% for SP-A60, SP-A45, and SP-A30 models, respectively.

The curves of SP-30 and SP-45 models gave an indication that the whole system was under pure yielding failure, while SP-A60 behavior indicated that the system was under pure yielding in the second phase, and under buckling in the third phase.

From the other side, all of the models were started to fail by material yielding near joints at the ends of most connected members. The necking of shaft tube members at the ends resulted in a significant reduction of the system efficiency. Such matter could be avoided if a new members connection technique was introduced without necking at the ends.

Results of finite element modelling at maximum load capacity of various models are clarified in Figure (). The Von Mises criterion was utilized to assess yielding areas occurred in models' parts. Contour map legends showing that members with white area (except the bottom joints balls) have stresses higher than 387 MPa, which is defined as the yield point of the steel material. While those parts of members colored with red were reached the yielding point. It is worth mentioning that all of the models began to fail near connection joints, followed by yielding of top mid shaft tubes (for SP-A30 and SP-A45). In the contrary to SP-A60, where all the diagonal members failed by yielding while the all top members remained within the elastic limit.

No clear buckling failure was observed for SP-A30 curves model, as can be noted for previous load-displacement curve. Where curve hardening behavior after the elastic limit remains with constant load while

increasing downward displacement. Unlike SP-A45, where a noticeable buckling point in the curve were observed for specific region followed by uniform degradation. In the other side, a very clear bucking behavior have noticed in load - displacement curve of SP-A60 model. The model could not withstand intended load for the specified deformation. Figure (12) clarifies models' deformation before and after applying load. It can be clearly observed that the deformation of diagonal members of SP-60 were strongly buckled at midspan compared with SP-A45, at the same displacement value.

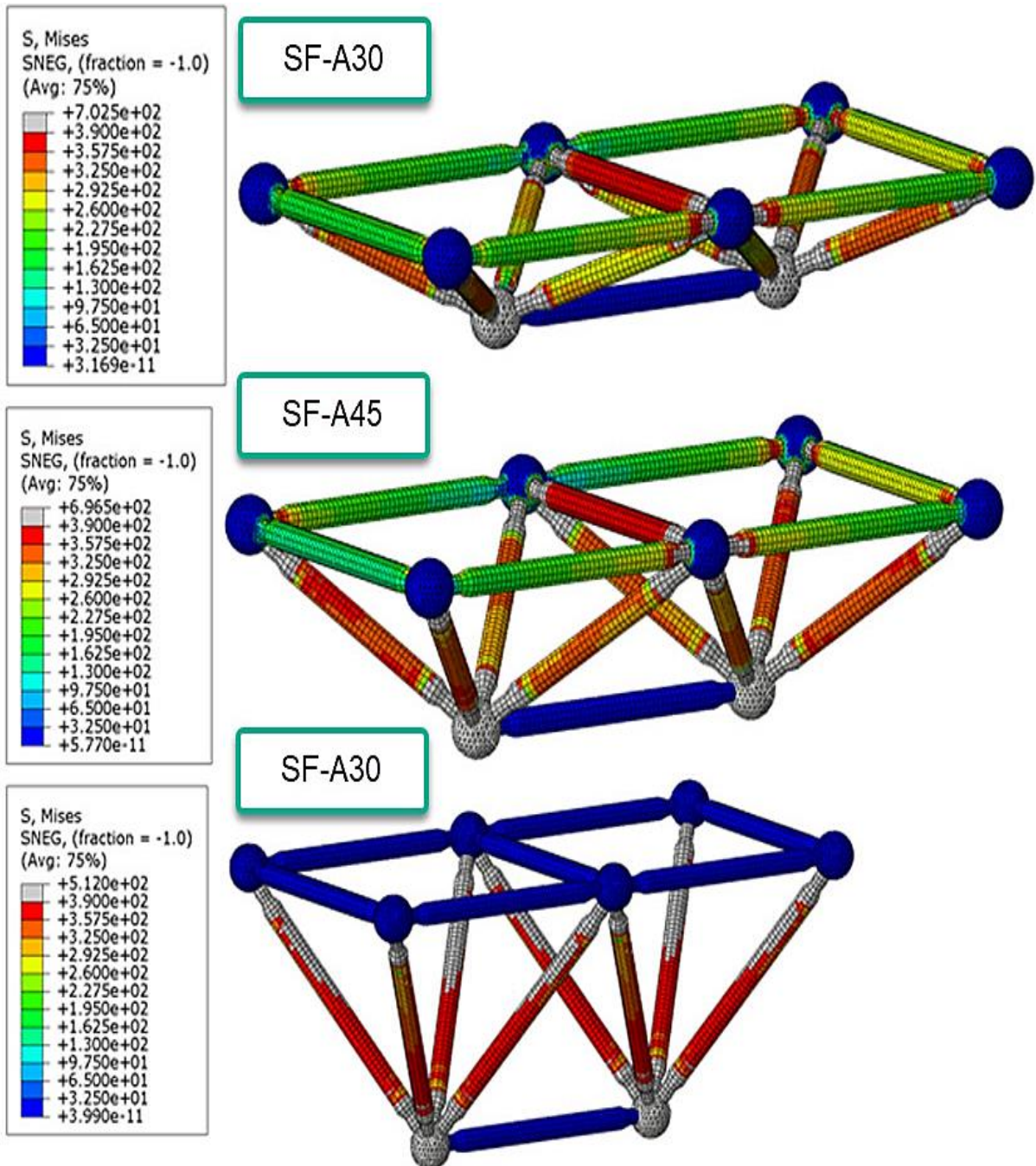


Figure 11. Von Misses stresses distribution map of SF model at maximum load

Due to the geometrical configuration and specialty of each model, the finite element results showed that when the angle of SF was 30 or 45, both main and diagonal members were loaded with specific amount of stresses. In the contract to SF-A60, where most of load transferred directly to the diagonal members, and that is why the SF-A60 showed different curve behavior due to sudden collapsing.

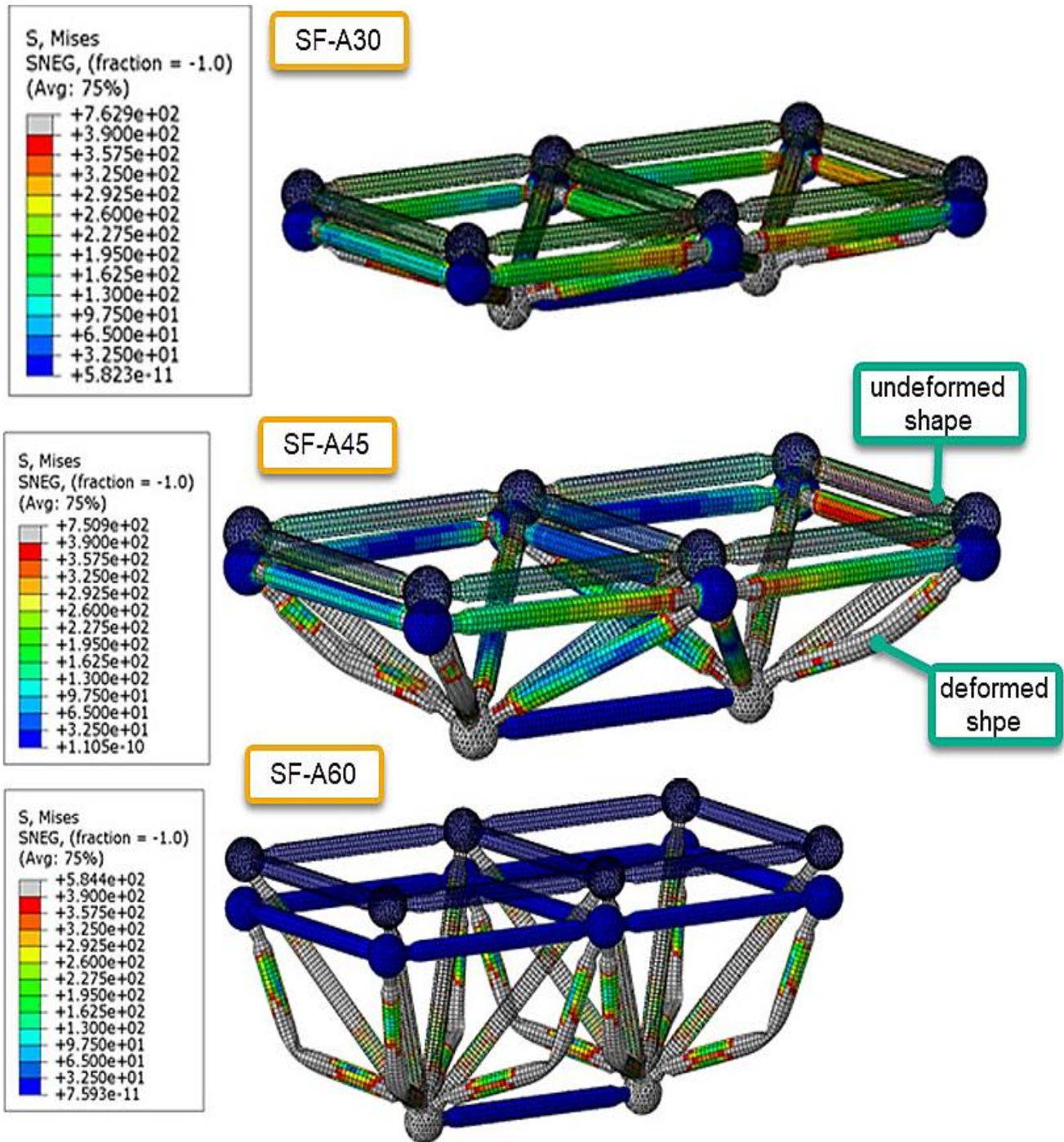


Figure 12. comparison between various collapsing shape SF models at failure

5. FEM results of composite spaceframes (CSFs)

FEM results in term of load – displacement curves for different models are illustrated in Figures (13,14, and 15). For type A-30 models, the CSF reflected lower initial stiffness, and slightly higher maximum load capacity compared to SF, where maximum capacity increased about 2.4%. in addition to a reduction in downward displacement at maximum load of about 81%, as can be seen in Figure (13). Also, a noticeable enhancement of about 7.7% was observed in maximum load capacity for CSF-A-45 compared to SF-A45, as illustrated in Figure (14). Further, about 50% of the strength still exist after 50 mm applied downward displacement. Also, the same

displacement values were observed at maximum load for both of the mentioned FE models.

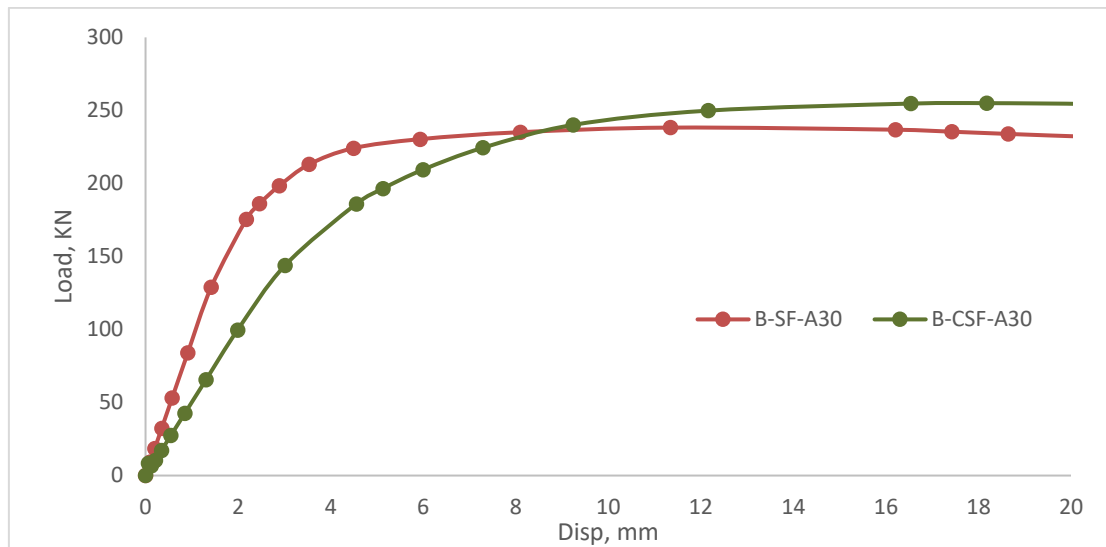


Figure 13. Comparison between SF-A30 and CSF-A30 in term of Load-Disp. Curves relation.

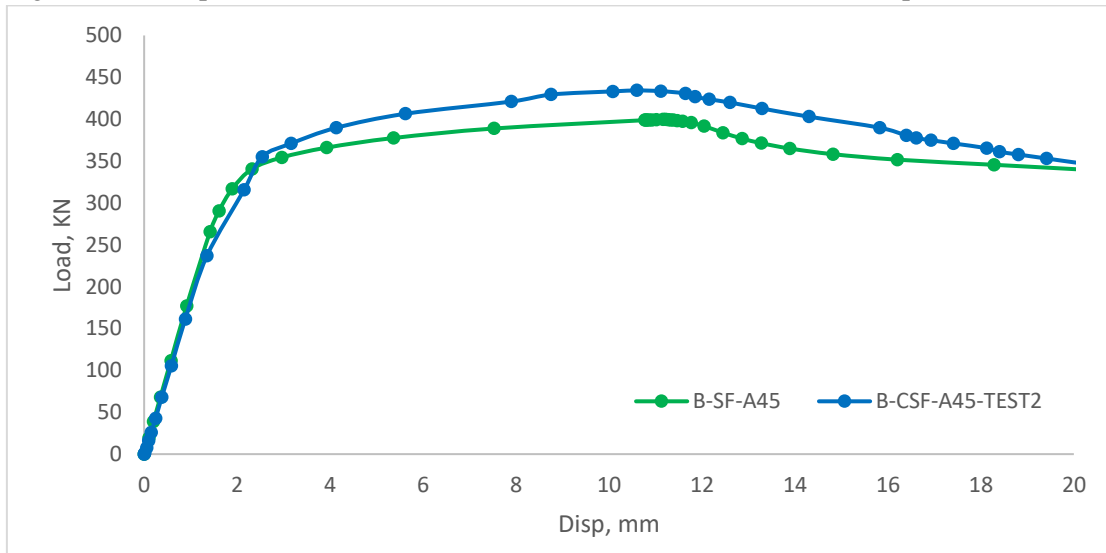


Figure 14. Comparison between SF-A45 and CSF-A45 in term of Load-Disp. Curves relation

In case of CSF-A60 model, although the same behavior in the elastic region was noticed relatively with SF-A60, the load carrying capacity were decreased about 6.28%, when relatively compared with SF-A60. On the other hand, a significant enhancement in whole system ductility were observed. Existence of concrete deck slab have constrained the whole system. The rule of concrete slab element may not clearly appear in A45 and A30 models. On the contrary to CSF-A60, where a significant enhancement in ductility and load carrying capacity degradation ratio.

A general comparison has been performed for all FEM models, in term of maximum load capacity, displacement at maximum load, toughness (ability of the system to absorb external work), and system stiffness (load capacity in KN per unit mm) as illustrated in Figures (16, 17, 18, and 19,). the comparison appears that load capacity of CSF-A60 and SF-A60 are comparable, and the highest among other models. While the maximum toughness value was observed for SF-A60, which was twice higher than CSF-A60 value. Which means that SF-A60 has the ability to absorb energy better than CSF-A60. the toughness of the CSF-A60 was the highest among other

models, and specifically 1.6 times higher than SF-A60.

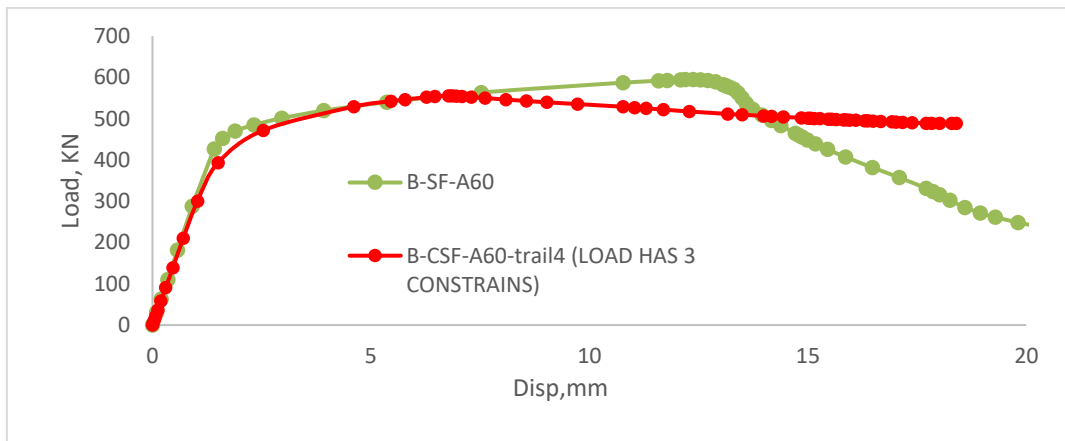


Figure 15. Comparison between SF-A60 and CSF-A60 in term of Load-Disp. Curves relation

In the other side, the ultimate load, displacement at max load, stiffness and toughens of CSF-A45 were comparable and slightly higher than SF-A45.

The SF-A30 showed comparable results to CSF-A30 in term of ultimate load, while the displacement at max load of CSF-A30 was higher about 2 times than CF-A30, and the toughness was higher 1.4 times. While the stiffness of CF-A30 was higher about 2 times of SF-A30.

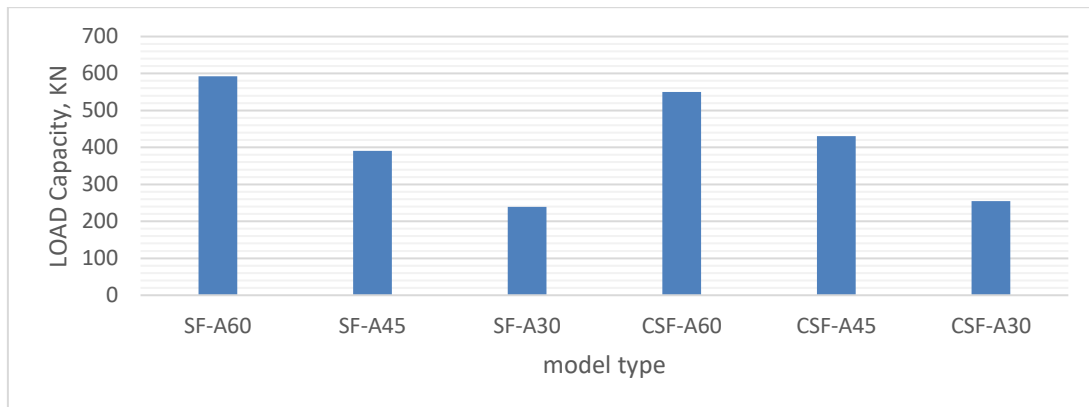


Figure 16. Maximum load capacity Comparison for various SFs and CSFs models

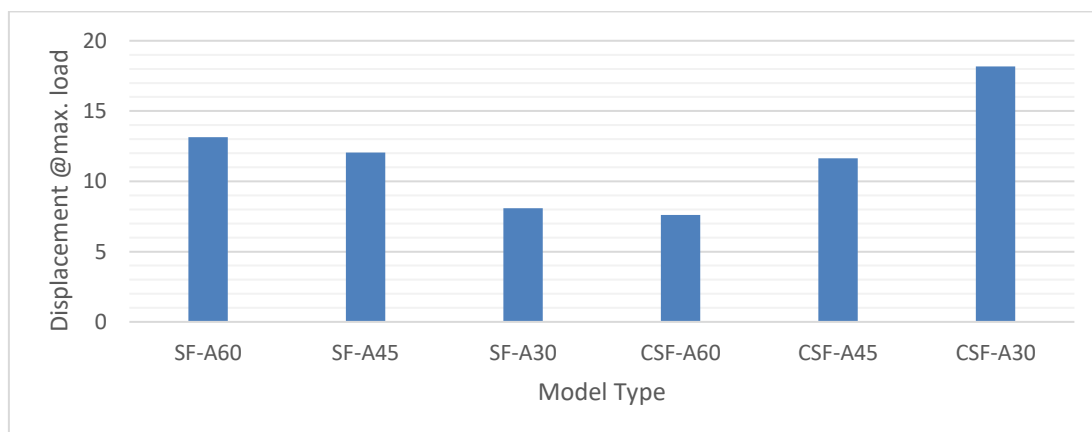


Figure 17. General comparison of models Downward Displacement at Maximum load capacity

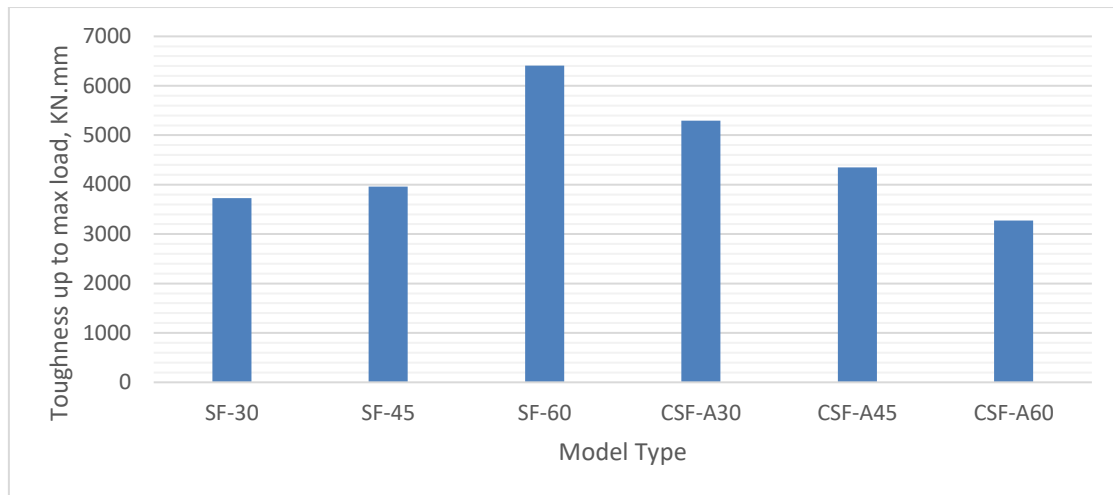


Figure 18: General comparison of models Toughness up to the Maximum load capacity

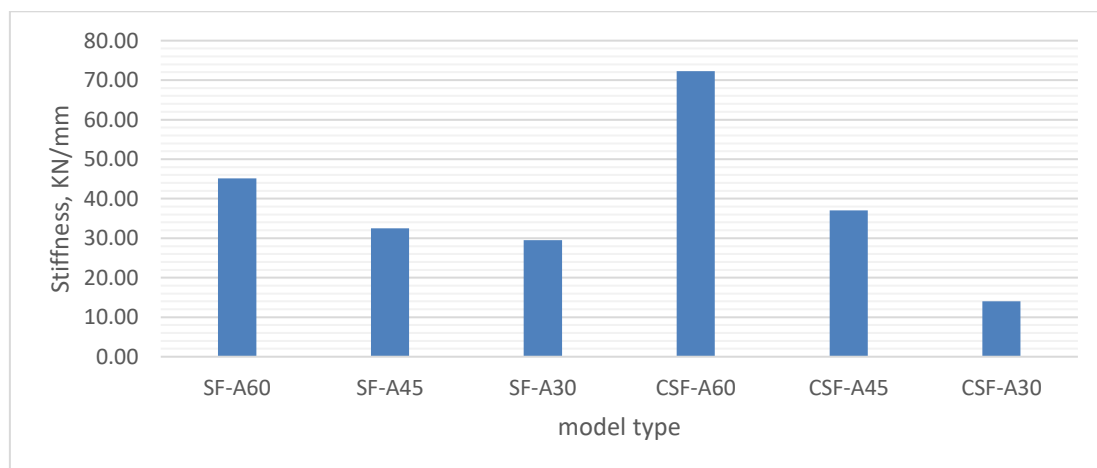


Figure 19: General comparison of models Stiffness up to the Maximum load capacity

6. Conclusion

based on the previously mentioned results and discussions, the following conclusions can be drawn:

1. Validity results have shown good agreement between FEM results and the experimental work, and go with both ultimate load and failure type.
2. Spaceframe model (conventional and composite) with angle 60 between members had the highest maximum load carrying capacity, and lowest ductility. In the contract to the Spaceframe with angle 30 which had the lowest maximum load can withstand, and highest ductility among other types.
3. The study aim was achieved for the new technique of composite spaceframe as its capacity were comparable to conventional spaceframes, which means the ability of the new system to work as (floor) system instead of its conventional use as (roof) system.
4. Increasing angle between members (or increasing spaceframes height) resulted in higher load can be carried by the system. On the other hand, such increase will not be safe because of buckling failure (the third phase), as observed in models with angle 60. balancing between load capacity and ductility may be necessary for structural systems to avoid any unexpected sudden failure. the systems with higher angle between member mean longer diagonal members, which is largely exposed to bucking failure rather than yielding of their material.
5. The necking area at the ends of each connected members near joints was the weakest point in the system since most of models have started to yield at this point.

6. Increasing model angle (height) resulted in different methods of load transfer. models' members with angle 30 and 45 have noticed that both main and diagonal type shared the load. In the contract to models with angle 60, where large percentage of the load transmitted to the diagonal parts directly.

References

- [1] J. J. S. g. s. CHILTON, "6 Deployable, foldable and retractable space grids," 2000.
- [2] Y. S. Hamid, *Progressive collapse of double layer space trusses*. University of Surrey (United Kingdom), 2015.
- [3] C. J. E. F. A. Vatansever, "Investigation of buckled truss bars of a space truss roof system," vol. 106, p. 104156, 2019.
- [4] O. Caglayan and E. J. E. F. A. Yuksel, "Experimental and finite element investigations on the collapse of a Mero space truss roof structure–A case study," vol. 15, no. 5, pp. 458-470, 2008.
- [5] F. Piroglu and K. J. E. F. A. Ozakgul, "Partial collapses experienced for a steel space truss roof structure induced by ice ponds," vol. 60, pp. 155-165, 2016.
- [6] F. Piroglu, K. Ozakgul, H. Iskender, L. Trabzon, and C. J. E. F. A. Kahya, "Site investigation of damages occurred in a steel space truss roof structure due to ponding," vol. 36, pp. 301-313, 2014.
- [7] A. Fülöp and M. J. T.-W. S. Iványi, "Experimentally analyzed stability and ductility behaviour of a space-truss roof system," vol. 42, no. 2, pp. 309-320, 2004.
- [8] C. D. Hill, G. E. Blandford, and S. T. J. J. o. S. E. Wang, "Post-buckling analysis of steel space trusses," vol. 115, no. 4, pp. 900-919, 1989.
- [9] E. A. J. J. o. S. E. Smith, "Space truss nonlinear analysis," vol. 110, no. 4, pp. 688-705, 1984.
- [10] J. Lubliner, J. Oliver, S. Oller, E. J. I. J. o. s. Oñate, and structures, "A plastic-damage model for concrete," vol. 25, no. 3, pp. 299-326, 1989.
- [11] J. Lee and G. L. J. J. o. e. m. Fenves, "Plastic-damage model for cyclic loading of concrete structures," vol. 124, no. 8, pp. 892-900, 1998.
- [12] D. M. H. Haitham H. Muteb, "Ultra-High-Performance Concrete Using Local Materials And Production Methods," *IOP Conference Series: Materials Science and Engineering*, no. IOP Conf. Ser.: Mater. Sci. Eng. 870 012100, 2020.
- [13] T. M. Ahlborn, D. K. Harris, D. L. Misson, and E. J. J. T. r. r. Peuse, "Characterization of strength and durability of ultra-high-performance concrete under variable curing conditions," vol. 2251, no. 1, pp. 68-75, 2011.
- [14] M. Shafieifar, M. Farzad, A. J. C. Azizinamini, and B. Materials, "Experimental and numerical study on mechanical properties of Ultra High Performance Concrete (UHPC)," vol. 156, pp. 402-411, 2017.
- [15] C. E. E.-i. D. B. Eton, *CEB-FIP Model Code 1990: Design Code*. T. Telford, 1993.
- [16] C. Gu, G. Ye, and W. J. S. C. T. S. Sun, "Ultrahigh performance concrete-properties, applications and perspectives," vol. 58, no. 4, pp. 587-599, 2015.
- [17] A. C. I. Committee, *Building code requirements for structural concrete : (ACI 318-14) ; and commentary (ACI 318R-14)*. Farmington Hills, MI : American Concrete Institute, [2014] ©2014, 2014.
- [18] T. Yu, J. Teng, Y. Wong, and S. J. E. s. Dong, "Finite element modeling of confined concrete-II: Plastic-damage model," vol. 32, no. 3, pp. 680-691, 2010.

- [19] T. Yu, J. Teng, Y. Wong, and S. J. E. S. Dong, "Finite element modeling of confined concrete-I: Drucker–Prager type plasticity model," vol. 32, no. 3, pp. 665-679, 2010.
- [20] S. Michał and W. Andrzej, "Calibration of the CDP model parameters in Abaqus," in *THE 2015 WOULD CONGRESS ON ADVANCES IN STRUCTURAL ENGINEERING AND MECHANICS (ASEM15)*, 2015.
- [21] L. J. J. o. p. v. t. James, "Ramberg–Osgood strain-hardening characterization on an ASTM A302-B steel," vol. 117, no. 4, pp. 341-345, 1995.
- [22] A. Niesłony, C. el Dsoki, H. Kaufmann, and P. J. I. J. o. F. Krug, "New method for evaluation of the Manson–Coffin–Basquin and Ramberg–Osgood equations with respect to compatibility," vol. 30, no. 10-11, pp. 1967-1977, 2008.
- [23] R. C. Rice, *Metallic Materials Properties Development and Standardization (MMPDS): Chapters 5-9 and appendices*. National Technical Information Service, 2003.
- [24] A. U. J. P. U. Manual, "Dassault Systèmes Simulia Corporation," 2010.
- [25] S. Chaudhari and M. J. I. J. o. C. A. Chakrabarti, "Modeling of concrete for nonlinear analysis using finite element code ABAQUS," vol. 44, no. 7, pp. 14-18, 2012.
- [26] A. S. Genikomsou and M. A. J. E. S. Polak, "Finite element analysis of punching shear of concrete slabs using damaged plasticity model in ABAQUS," vol. 98, pp. 38-48, 2015.
- [27] Z. Fan, G. Lu, and K. J. E. S. Liu, "Quasi-static axial compression of thin-walled tubes with different cross-sectional shapes," vol. 55, pp. 80-89, 2013.